of a real-space approach with the possibility of working directly with the measured data as typical in reciprocal-space methods.

3.6.3. Examples of WPPM analysis

To illustrate the power of the WPPM approach, a few examples are provided based both on simulated and on real data. The analyses were performed using the *PM2K* software (Leoni *et al.*, 2006). Similar results are obtained using the WPPM implementation in the commercial program *TOPAS*.

3.6.3.1. *Nanocrystalline ceria*

The first example concerns a nanocrystalline ceria powder obtained by the calcination of a cerium isopropoxide gel (Leoni, Di Maggio *et al.*, 2004; Leoni & Scardi, 2004; Scardi *et al.*, 2004). A large amount of XRD and transmisson electron microscopy (TEM) data have been collected on the same system (and specimen), starting from the xerogel and following calcination (Scardi *et al.*, 2010). Fig. 3.6.1(*a*) shows the X-ray powder diffraction pattern of the gel calcined for 1 h at 673 K measured with Cu radiation (40 kV, 45 mA) on a Rigaku PMG/VH diffractometer.

The data were collected over the 2θ range 18–154° (with a step of 0.05°) with a counting time of 60 s per step: a wide angular range and a high signal-to-noise ratio (SNR) are prerequisites for a proper line-profile analysis. The large span in reciprocal space is important for the complete characterization of any anisotropy in the broadening (a large set of independent directions in reciprocal space needs to be sampled), whereas the high SNR guarantees the collection of data at peak tails where the differences between similar microstructure models manifest themselves. The log scale employed in Fig. 3.6.1(*a*) highlights the low level of noise present in the pattern.

The diffractometer had 0.5° divergence and 2° Soller slits mounted on the primary arm and 0.15 mm antiscatter, 0.5° receiving and 2° Soller slits and a curved graphite analyzer crystal mounted on the secondary arm. This setup provided a narrow and symmetrical instrumental profile that could be described by a pseudo-Voigt curve and was thus ideal for line-profile analysis studies. The Caglioti *et al.* (1958) parameterization of the instrumental profile [*cf.* equations (3.6.18) and (3.6.19)] performed on the profiles of the NIST SRM 660a standard (LaB_6) is shown in Fig. 3.6.2.

Analysis of the pattern using traditional methods (see Scardi *et al.*, 2004) required 59 parameters, 53 of which were actually refined:

(i) one unit-cell parameter (a_0),
(ii) six (fixed) parameters defining the instrumental contribution [five parameters for the Caglioti parameterization (U, V, W, a and b) and one for the $K\alpha_2$ intensity ratio],
(iii) three parameters for the background,
(iv) one parameter for the specimen displacement,
(v) 48 parameters for the peaks (intensity, FWHM and shape for 16 peaks).

An analysis using traditional analysis methods resulted in an 'average domain size' of 3.65 (10) nm using the (modified) Warren–Averbach method and in the range from 4.95 (10) to 5.3 (1) nm using a (modified) Williamson–Hall approach. A discussion of the meaning and accuracy of the results can be found in Scardi *et al.* (2004).

The WPPM result, shown in Fig. 3.6.1(*b*), matches the experiment quite well: this is remarkable considering that the whole pattern (1800 data points) is modelled using just 32 parameters (26 free parameters):

(i) one unit-cell parameter (a_0),
(ii) six (fixed) parameters defining the instrumental contribution [five parameters for the Caglioti parameterization (U, V, W, a and b) and one for the $K\alpha_2$ intensity ratio],

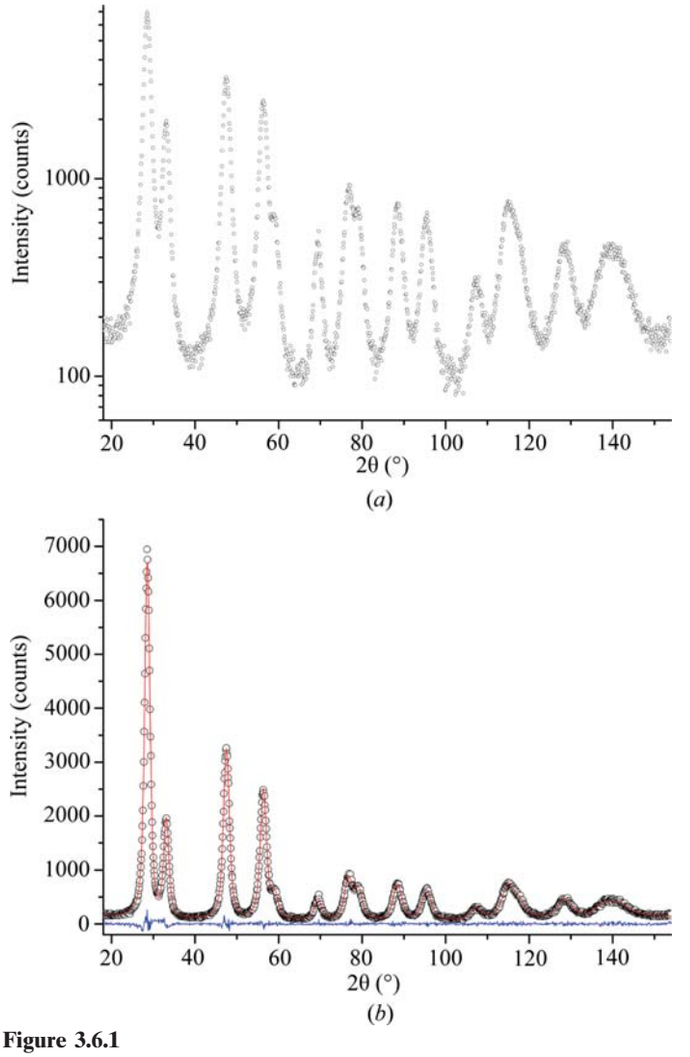

Figure 3.6.1
X-ray powder diffraction pattern of nanocrystalline ceria calcined at 673 K. In (*a*) the pattern is shown on a log scale to highlight the weak features in the data. In (*b*) the results of WPPM are shown: raw data (dots), model (line) and difference (lower line).

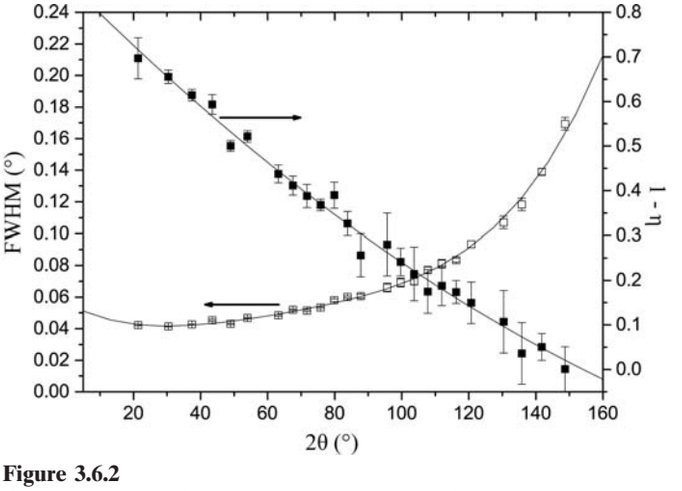

Figure 3.6.2
Parameterization of the instrumental resolution function using a pseudo-Voigt and the relationship of Caglioti *et al.* (1958).

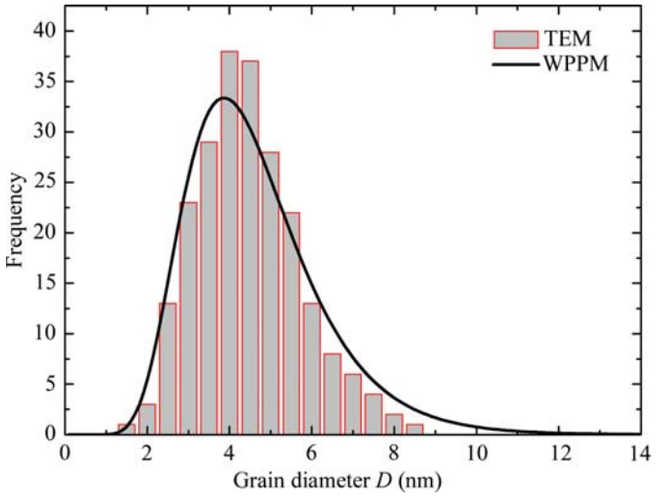

Figure 3.6.3
Size distribution of the ceria powder: WPPM (line) and TEM (histogram).

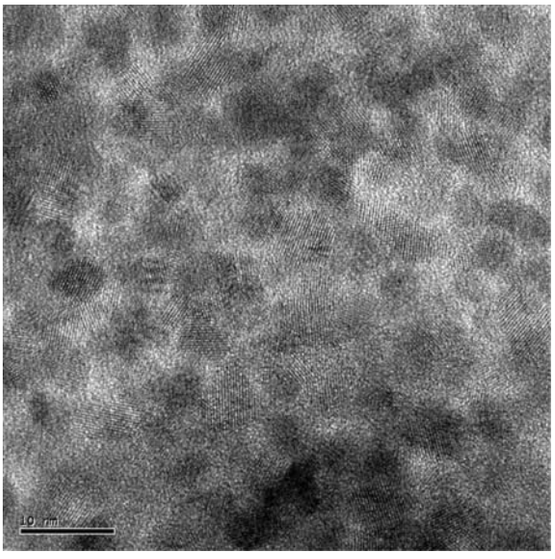

Figure 3.6.4
TEM micrograph of the calcined ceria powder. The scale bar represents 10 nm.

(iii) two parameters for the log-normal size distribution (μ and σ),
(iv) three parameters for the dislocation contributions (ρ, R_e and the mixing parameter f_e),
(v) three parameters for the background,
(vi) one parameter for the specimen displacement,
(vii) 16 parameters for the intensity of the peaks.

It is therefore possible to obtain more complete results with a number of parameters that is dramatically lower than that needed for the traditional analysis: the shapes of the peaks are interlinked *via* the microstructure models. It is suggested that the parameters are initialized with values providing a minimal but measurable effect (*i.e.*, for instance, $\mu = 2$, $\sigma = 0.4$, $\rho = 10^{15}$ m^{-2}, $f_e = 0.5$) to favour a rapid convergence.

By way of a check, Fig. 3.6.3 shows the good agreement between the size distribution obtained by WPPM and that obtained on the same specimen from the analysis of a large set of TEM micrographs (800 grains surveyed; Fig. 3.6.4). The data were collected on a 300 kV JEOL 3010 microscope (0.17 nm point-to-point resolution) equipped with a Gatan slow-scan 974 CCD camera (Leoni, Di Maggio *et al.*, 2004). Even if the particles are well separated, the analysis is quite tedious and prone to bias from the operator. The large and small particles are in fact easily missed, and overlapping particles are hard to separate and are usually not considered. Moreover, only the cross section is measured, as the transverse direction is difficult to access.

The statistical validity of the WPPM result is quite clear: a few million grains are probed by the X-rays *versus* the few hundred actually considered in microscopy. The WPPM result allows not only the mean (first moment) and variance to be obtained from the refined size distribution, but also the recovery of the most probable values for the traditional results (we know the shape and we can weight the column-length distribution by the surface or by the volume). In this case the numerical mean is ~4.3 nm: we can immediately understand the risk of placing faith in the results of a traditional analysis. The agreement between TEM and XRD is in any case excellent. The residual differences may be due both to the issues related to sizing under the microscope and to the simplified treatment employed in the WPPM (perfectly spherical domains, monodisperse shape, absence of surface relaxation *etc.*). A more complex model (accounting, for example, for surface relaxation effects) can be considered (see Scardi & Leoni, 2002; Leoni & Scardi, 2004), but the effects on the distribution are minimal.

The possibility of extracting information on the type of defects (*e.g.* dislocations, faults and APDBs) and on their amount is definitely a major advantage of WPPM over traditional methods and over TEM. For the determination of the dislocation density, the average contrast factor is needed; the actual expressions can be readily obtained from the single-crystal elastic constants (c_{11} = 403, c_{12} = 105 and c_{44} = 60 GPa; Nakajima *et al.*, 1994) as

$$\overline{C}_{\mathrm{CeO_2},e} = 0.122945 + 0.358092\frac{h^2k^2 + k^2l^2 + h^2l^2}{(h^2 + k^2 + l^2)^2}, \qquad (3.6.54)$$

$$\overline{C}_{\mathrm{CeO_2},s} = 0.105762 + 0.207999\frac{h^2k^2 + k^2l^2 + h^2l^2}{(h^2 + k^2 + l^2)^2} \qquad (3.6.55)$$

for edge and screw dislocations, respectively.

A dislocation density of 1.4×10^{16} m^{-2} was obtained for the specimen analysed here. This dislocation density immediately appears to be quite high when compared with the number of dislocations that can be identified in high-resolution TEM micrographs, as it corresponds to approximately one dislocation every couple of grains (Leoni & Scardi, 2004). However, the dislocations visible in the micrographs are just a small fraction of the total: if a dislocation is not properly aligned with the zone axis, it is in fact invisible (its presence can only be inferred from the effects of the distortion field). It is true that a sufficiently large number of dislocations must be present in order to give appreciable effects on the diffraction pattern, and TEM is still the better technique if the density of dislocations is below, for example, 10^{14} m^{-2}.

3.6.3.2. *Copper oxide*

The true power of WPPM, and of diffraction in general, can be appreciated in multi-phase systems. The unequivocal assignment of a structure to each grain is definitely impossible using TEM, unless each grain is individually sampled and carefully analysed. It is therefore quite hard to identify the phases present in the specimen and to characterize their microstructure independently from a micrograph alone. Conversely, information on the various phases is well separated in a diffraction pattern. The various (known) phases in a specimen can easily be identified (for

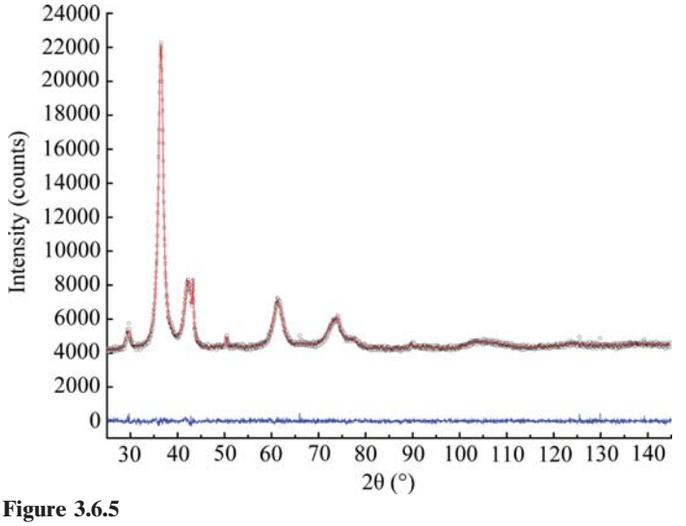

Figure 3.6.5
Result of WPPM of ball-milled Cu_2O: raw data (dots), model (line) and difference (lower line).

example by search/match in a large database such as the ICDD Powder Diffraction File): each diffraction peak belongs to a well defined phase and bears information on the microstructure of that phase.

As an example, Fig. 3.6.5 shows the diffraction pattern of a Cu_2O powder specimen obtained by grinding commercial Cu_2O powder (Carlo Erba) in a high-energy shatter mill (Fritsch Pulverisette 9). To limit the heating of the cup that would lead to dynamic recrystallization, milling was performed in 30 steps consisting of 10 s milling followed by 120 s room-temperature cooling (Martinez-Garcia *et al.*, 2007). The powder diffraction pattern was collected on the same diffractometer that was used for the analysis of the ceria powder. To obtain a sufficient SNR, the data were collected in the 18–154° 2θ range with a step size of 0.1° and a fixed acquisition time of 150 s per point. The fluorescence of the Cu present in the specimen is responsible for the large background that was not eliminated by the crystal analyser. From a quick comparison of Figs. 3.6.5 and 3.6.1, we notice a large difference at high angle: high strain effects (due to dislocations) are expected in this specimen as an effect of the extensive cold-work deformation introduced by the milling process.

A search match signals the presence of not just Cu_2O (cuprite, $Pn\bar{3}m$) but also metallic Cu (f.c.c. copper, $Fm\bar{3}m$) and CuO (tenorite, Cc) as minor phases, presumably due to reduction of the higher oxide. WPPM of the diffraction pattern, performed by considering all three observed phases, shows a flat residual (see Fig. 3.6.5). The severe peak overlap and the large broadening at high angle do not help in the analysis: the intensities of tenorite peaks (minor and broadened phase) were then constrained by a structural model (only a scale parameter was refined). Atomic coordinates and Debye–Waller factors for CuO were taken from the ICSD file (FIZ#69094; Brese *et al.*, 1990) and were considered to be constant.

Spherical domains were chosen for all phases. A log-normal distribution was used to model the minor phases. A histogram distribution was chosen for cuprite instead: the peaks clearly have a peculiar shape with a rather sharp tip, possibly indicating a wide, bimodal or odd size distribution (Leoni & Scardi, 2004). The size distribution resulting from the WPPM analysis is shown in Fig. 3.6.6(a): in this case it would be impossible for a traditional method to provide a physically sound result. The breadth of the profile is not fully informative: as the diffraction signal is proportional to the volume of matter, the actual distribution

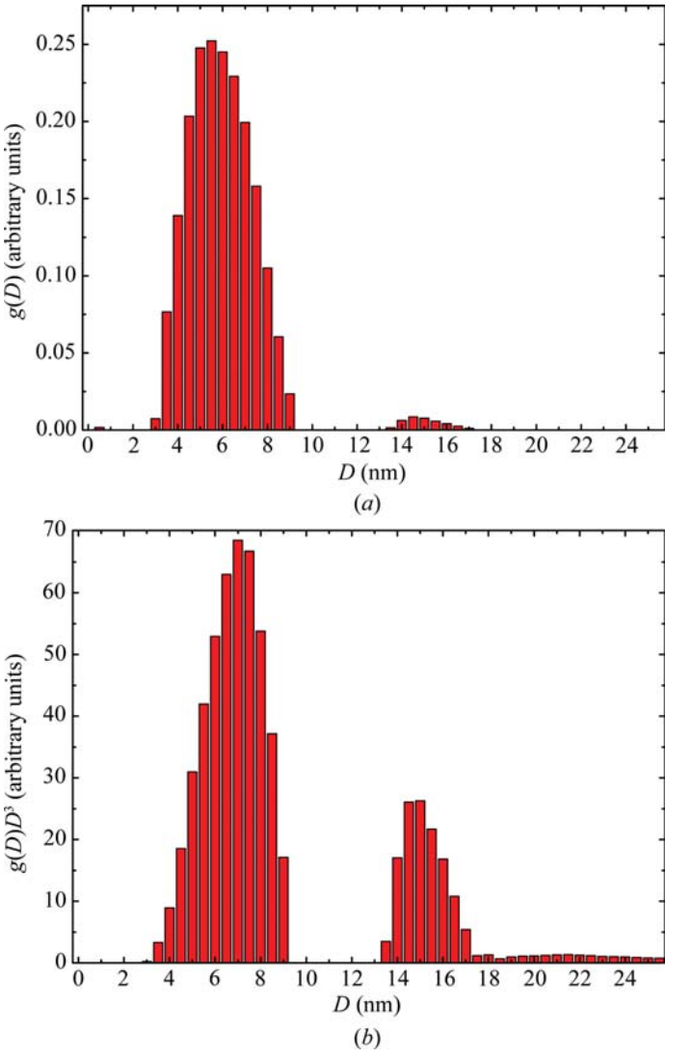

Figure 3.6.6
Domain-size distribution of cuprite: (a) WPPM result and (b) distribution multiplied by D^3.

'seen' in the experiment is that of Fig. 3.6.6(b), obtained by multiplying the result of Fig. 3.6.5(a) by D^3.

The larger size fraction therefore makes a non-negligible contribution to the pattern: as a rule of thumb, the smaller the domains and the wider the distribution, the stronger the contribution of the large domains. This problem of 'visibility' of small domains is attenuated when an analytical distribution (*e.g.* a log normal) can be used as the function goes smoothly to zero at zero size.

Dislocations can also be observed in these specimens: their quantification by TEM is nearly impossible due to the high defect density. The anisotropy term, *i.e.* the average contrast factor, has to be calculated for each of the three phases (Scardi *et al.*, 2007).

The slip system for Cu (c_{11} = 169, c_{12} =122, c_{44} = 75.3 GPa; Every & McCurdy, 1992a) is $\frac{1}{2}\langle 1\bar{1}0\rangle\{111\}$ and the corresponding average contrast factor (for edge and screw dislocations, respectively), is

$$\overline{C}_{\mathrm{Cu},e} = 0.304062 - 0.500211\,\frac{h^2k^2 + k^2l^2 + h^2l^2}{(h^2 + k^2 + l^2)^2}, \qquad (3.6.56)$$

$$\overline{C}_{\mathrm{Cu},s} = 0.298340 - 0.708805\,\frac{h^2k^2 + k^2l^2 + h^2l^2}{(h^2 + k^2 + l^2)^2}. \qquad (3.6.57)$$

For cuprite, the literature (Tromans & Meech, 2001) suggests that the main slip system is ⟨001⟩{100}. The contrast factor can be calculated analytically from the single-crystal elastic constants of cuprite (c_{11} = 121, c_{12} = 105 and c_{44} = 12.1 GPa; Every & McCurdy, 1992*b*) following Martinez-Garcia *et al.* (2007):

$$\overline{C}_{\mathrm{Cu_2O},e} = 0.355963 - 0.609491\,\frac{h^2k^2 + k^2l^2 + h^2l^2}{(h^2 + k^2 + l^2)^2}, \quad (3.6.58)$$

$$\overline{C}_{\mathrm{Cu_2O},s} = \frac{2}{3}\frac{h^2k^2 + k^2l^2 + h^2l^2}{(h^2 + k^2 + l^2)^2}. \quad (3.6.59)$$

For tenorite, a different approach was followed. The phase is minor and the single-crystal elastic constants are not readily available: we can therefore use the contrast factor in an effective way by refining the coefficients of the corresponding invariant [see equation (3.6.42)]. This preserves the profile shape determined by Wilkens' theory and just dilutes the meaning of the dislocation density. The average contrast factor is

$$\begin{aligned}\overline{C}_{\mathrm{CuO},\{hkl\}} &= \Big\{4\big[E_1h^4 + E_2k^4 + E_3l^4 + 2(E_4h^2k^2 + E_5k^2l^2 + E_6h^2l^2) \\ &\quad + 4(E_7h^3k + E_8h^3l + E_9k^3h)\big]Y^4Z^4\sin^4\beta\Big\} \\ &\quad \times \Big(\big\{k^2Z^2 + 2Y^2(l^2 + h^2Z^2) - Z[4hlY^2\cos(\beta) + k^2Z\cos(2\beta)]\big\}^2\Big)^{-1}, \end{aligned} \quad (3.6.60)$$

where a, b, c and β are the unit-cell parameters of tenorite, $Y = b/a$ and $Z = c/a$.

The dislocation density in Cu_2O is quite high [ρ = 2.8 (5) × 10^{16} m^{-2}]: dislocations are more of the edge character [f_E = 0.85 (3)] and the outer cutoff radius R_e = 9 (3) nm leads to a Wilkens' parameter of approximately 1.5, suggesting a strong dislocation interaction. The high dislocation density in this material is justified by the very low shear modulus (G = 10.3 GPa; Every & McCurdy, 1992*b*), whereas the high dislocation interaction is the result of the severe deformation induced by the milling.

APPENDIX A3.6.1
Functions for profile shapes

The unit-area Gaussian $G(x, \omega)$ and Lorentzian $L(x, \omega)$ functions are defined as

$$G(x, \omega) = \frac{2\sqrt{\ln 2/\pi}}{\omega}\exp\left(-\frac{4x^2\ln 2}{\omega^2}\right), \quad (3.6.61)$$

$$L(x, \omega) = \frac{2}{\pi\omega}\left(\frac{1}{1 + 4x^2/\omega^2}\right), \quad (3.6.62)$$

where x is the running variable and ω is the full-width at half-maximum. Based on these definitions, the Voigt and pseudo-Voigt are

$$V(x, \omega_L, \omega_G) = L(x, \omega_L) \otimes G(x, \omega_G) \quad (3.6.63)$$

and

$$\mathrm{pV}(x, \omega_L, \omega_G) = \eta L(x, \omega_L) + (1 - \eta)G(x, \omega_G), \quad (3.6.64)$$

respectively, where η is the mixing parameter (ranging between 0 and 1) and w_L and w_G are the width of the Lorentzian and Gaussian components, respectively.

References

Adler, T. & Houska, C. R. (1979). *Simplifications in the X-ray line-shape analysis. J. Appl. Phys.* **50**, 3282–3287.

Alexander, L. (1954). *The synthesis of X-ray spectrometer line profiles with application to crystallite size measurements. J. Appl. Phys.* **25**, 155–161.

Armstrong, N., Leoni, M. & Scardi, P. (2006). *Considerations concerning Wilkens' theory of dislocation line-broadening. Z. Kristallogr. Suppl.* **23**, 81–86.

Balogh, L., Ribárik, G. & Ungár, T. (2006). *Stacking faults and twin boundaries in fcc crystals determined by X-ray diffraction profile analysis. J. Appl. Phys.* **100**, 023512.

Balzar, D. & Popović, S. (1996). *Reliability of the simplified integral-breadth methods in diffraction line-broadening analysis. J. Appl. Cryst.* **29**, 16–23.

Bergmann, J. & Kleeberg, R. (2001). *Fundamental parameters versus learnt profiles using the Rietveld program BGMN. Mater. Sci. Forum*, **378–381**, 30–37.

Berkum, J. G. M. van (1994). *Strain Fields in Crystalline Materials*. PhD thesis, Technische Universiteit Delft, Delft, The Netherlands.

Bertaut, E. F. (1949*a*). *Etude aux rayons X de la répartition des dimensions des cristallites dans une poudre cristalline. C. R. Acad. Sci.* **228**, 492–494.

Bertaut, E. F. (1949*b*). *Signification de la dimension cristalline mesurée d'apres la largeur de raie Debye-Scherrer. C. R. Acad. Sci.* **228**, 187–189.

Bertaut, E. F. (1950). *Raies de Debye–Scherrer et repartition des dimensions des domaines de Bragg dans les poudres polycristallines. Acta Cryst.* **3**, 14–18.

Beyerlein, K. R., Leoni, M. & Scardi, P. (2012). *Temperature diffuse scattering of nanocrystals. Acta Cryst.* A**68**, 382–392.

Billinge, S. J. L. (2008). *Local structure from total scattering and atomic pair distribution function (PDF) analysis.* In *Powder Diffraction: Theory and Practice*, edited by R. E. Dinnebier & S. J. L. Billinge. London: Royal Society of Chemistry.

Brese, N. E., O'Keeffe, M., Ramakrishna, B. L. & Von Dreele, R. B. (1990). *Low-temperature structures of CuO and AgO and their relationships to those of MgO and PdO. J. Solid State Chem.* **89**, 184–190.

Bruker (2009). *DIFFRAC.SUITE TOPAS*, *Total Pattern Analysis Solution.* Version 5. Bruker AXS, Karlsruhe, Germany.

Caglioti, G., Paoletti, A. & Ricci, F. P. (1958). *Choice of collimator for a crystal spectrometer for neutron diffraction. Nucl. Instrum.* **3**, 223–228.

Cervellino, A., Giannini, C. & Guagliardi, A. (2003). *Determination of nanoparticle structure type, size and strain distribution from X-ray data for monatomic f.c.c.-derived non-crystallographic nanoclusters. J. Appl. Cryst.* **36**, 1148–1158.

Cheary, R. W. & Coelho, A. (1992). *A fundamental parameters approach to X-ray line-profile fitting. J. Appl. Cryst.* **25**, 109–121.

Cheary, R. W. & Coelho, A. (1994). *Synthesizing and fitting linear position-sensitive detector step-scanned line profiles. J. Appl. Cryst.* **27**, 673–681.

Cheary, R. W. & Coelho, A. A. (1998*a*). *Axial divergence in a conventional X-ray powder diffractometer. I. Theoretical foundations. J. Appl. Cryst.* **31**, 851–861.

Cheary, R. W. & Coelho, A. A. (1998*b*). *Axial divergence in a conventional X-ray powder diffractometer. II. Realization and evaluation in a fundamental-parameter profile fitting procedure. J. Appl. Cryst.* **31**, 862–868.

Cline, J. P., Black, D., Windover, D. & Henins, A. (2010). *SRM 660b – Line Position and Line Shape Standard for Powder Diffraction.* https://www-s.nist.gov/srmors/view_detail.cfm?srm=660b.

Coelho, A. A. (2005). *A bound constrained conjugate gradient solution method as applied to crystallographic refinement problems. J. Appl. Cryst.* **38**, 455–461.

Coelho, A. A. (2009). *TOPAS Academic.* Version 5. http://www.topas-academic.net/.

Cozzoli, P. D., Snoeck, E., Garcia, M. A., Giannini, C., Guagliardi, A., Cervellino, A., Gozzo, F., Hernando, A., Achterhold, K., Ciobanu, N., Parak, F. G., Cingolani, R. & Manna, L. (2006). *Colloidal synthesis and characterization of tetrapod-shaped magnetic nanocrystals. Nano Lett.* **6**, 1966–1972.

Debye, P. (1915). *Zerstreuung von Röntgenstrahlen. Ann. Phys.* **351**, 809–823.